



<b>Publication Year</b>	2018
<b>Acceptance in OA</b>	2020-09-29T09:16:32Z
<b>Title</b>	The Recoiling Black Hole Candidate 3C 186: Spatially Resolved Quasar Feedback and Further Evidence of a Blueshifted Broad-line Region
<b>Authors</b>	Chiaberge, Marco, Tremblay, Grant R., CAPETTI, Alessandro, Norman, Colin
<b>Publisher's version (DOI)</b>	10.3847/1538-4357/aac48b
<b>Handle</b>	<a href="http://hdl.handle.net/20.500.12386/27513">http://hdl.handle.net/20.500.12386/27513</a>
<b>Journal</b>	THE ASTROPHYSICAL JOURNAL
<b>Volume</b>	861



# The Recoiling Black Hole Candidate 3C 186: Spatially Resolved Quasar Feedback and Further Evidence of a Blueshifted Broad-line Region

Marco Chiaberge<sup>1,2</sup>, Grant R. Tremblay<sup>3</sup>, Alessandro Capetti<sup>4</sup>, and Colin Norman<sup>1,2</sup>

<sup>1</sup>Space Telescope Science Institute, 3700 San Martin Drive, Baltimore, MD 21218, USA; [marcoc@stsci.edu](mailto:marcoc@stsci.edu)

<sup>2</sup>Johns Hopkins University—Center for Astrophysical Sciences, 3400 N. Charles Street, Baltimore, MD 21218, USA

<sup>3</sup>Harvard-Smithsonian Center for Astrophysics, 60 Garden Street, Cambridge, MA 02138, USA

<sup>4</sup>INAF-Osservatorio Astrofisico di Torino, Via Osservatorio 20, I-10025, Pino Torinese, Italy

Received 2018 March 12; revised 2018 May 3; accepted 2018 May 12; published 2018 July 2

## Abstract

We present the results of integral field spectroscopy of the gravitational wave (GW) recoiling black hole candidate 3C 186. The goal of the observation is to study the kinematics of the [O III]5007 narrow emission-line region (NLR) of the quasar, and investigate the origin of the velocity offsets originally measured for different UV lines. The results show that (i) the spatial structure of the NLR is complex. The [O III]5007 line shows significant velocity offsets with respect to the systemic redshift of the source. Different components at different velocities ( $-670$ ,  $-100$ ,  $+75$  km s<sup>-1</sup>) are produced in different regions of the source. (ii) We detect both the narrow and the broad components of the H $\beta$  line. The narrow component generally follows the kinematics of the [O III] line, while the broad component is significantly blueshifted. The peak of the broad line is near the blue end, or possibly outside of the sensitivity band of the instrument, implying a velocity offset of  $\gtrsim 1800$  km s<sup>-1</sup>. This result is in agreement with the interpretation of the quasar as a GW recoiling black hole. The properties of the NLR show that the observed outflows are most likely the effect of radiation pressure on the (photoionized) gas in the interstellar medium of the host galaxy.

*Key words:* galaxies: active – galaxies: jets – gravitational waves – quasars: individual (3C 186)

## 1. Introduction

Supermassive black holes (SMBHs) may grow through accretion of matter during short-lived active phases, and/or via mergers. SMBH mergers are expected to occur as a result of major galaxy mergers, on timescales that may be as short as 10 Myr, depending on the properties of the gas in the merging galaxies, as shown by recent simulations (see Mayer 2017, for a recent review). An intimate relationship between galaxy growth and black hole growth also seems to be required to explain tight relationships such as the  $M$ – $\sigma$  correlation, originally discovered by Ferrarese & Merritt (2000) and Gebhardt et al. (2000). When galaxies merge, the two central SMBH first lose energy by dynamical friction, then by three-body interactions with stars that have appropriate angular momentum in the region of the parameter space (the so-called loss cone; Begelman et al. 1980). The pair keeps scattering stars off until it becomes sufficiently tightly bound that gravitational radiation is the most efficient mechanism responsible for energy and angular momentum losses. If SMBH bound pairs routinely form as a result of galaxy mergers, a stochastic gravitational wave (GW) background formed by the superposition of the low-frequency GW from each of these systems is also expected. Pulsar timing array (PTA) experiments (Hobbs 2013; Kramer & Champion 2013; McLaughlin 2013) and, in the future, space based GW observatories such as LISA (Amaro-Seoane et al. 2017) are built to be sensitive to such low-frequency GW emission. The details of the mechanisms that pull the two BHs to the distance at which GW emission becomes substantial are still poorly understood. A gas-rich environment may significantly help this process. Recent work using simulations show that even in gas-poor environments SMBH binaries can merge under certain conditions, e.g., if they formed in major galaxy mergers where

the final galaxy is non-spherical (Khan et al. 2011, 2012; Preto et al. 2011; Bortolas et al. 2016, and references therein). However, characteristic timescales to replenish the loss cone may be longer than a Hubble time. If the loss cone is not replenished quickly enough for the pair to get sufficiently close and lose energy via GWs, the pair may stall and never merge. Since the typical distance at which a pair with  $M_1 \sim M_2 \sim 10^7 M_\odot$  starts to efficiently shrink via GW emission is  $\sim 1$  pc, this is known as the final parsec problem (Milosavljević & Merritt 2003).

Recently, stringent upper limits on the GW background radiation derived with the Parkes PTA were interpreted as being in tension with the current paradigm of galaxy merger and SMBH pair formation (Shannon et al. 2015), but alternative scenarios that may remove such a tension were also proposed (Middleton et al. 2018; Rasskazov & Merritt 2017). The lack of PTA detections may imply that the timescales for the pairs to merge is either much shorter or much longer than expected. In the latter case, it could indicate that the final parsec problem indeed constitutes an issue. Detecting GW radiation from “stalled” SMBH pairs corresponds to the so-called “nightmare scenario” (Dvorkin & Barausse 2017). More broadly, if this prevents SMBH to merge, our current understanding on the mechanisms for black hole growth might need significant revisions. It is therefore extremely important to find (either direct, through GW detectors, or indirect) evidence of SMBH mergers, especially for black holes of very high mass ( $10^8$ – $10^9 M_\odot$ ).

One possible way to obtain observational evidence of SMBH mergers using electromagnetic radiation is to look for runaway (kicked) black holes. Depending on the properties (mass, spin) of each of the SMBH in a merging pair, the resulting merged black hole may get a kick and be ejected at velocities that can be, in principle, as high as the escape velocity of the host

galaxy (Madau & Quataert 2004; Merritt et al. 2004; Komossa 2012). This process has been extensively studied with numerical simulations (Campanelli et al. 2007; Blecha et al. 2011, 2016; Gerosa et al. 2018; Healy & Lousto 2018), but we are still lacking a confirmed example of such a phenomenon. If the ejected black hole is active, we could in principle observe both an offset active galactic nucleus (AGN) and velocity shifts between narrow and broad lines (Loeb 2007; Volonteri & Madau 2008). Such shifts are expected because the broad-line emitting region is dragged out with the kicked black hole, while the narrow-line region remains in the framework of the host galaxy. A few candidates have been reported so far in the literature, but equally plausible alternative interpretations for these observations are still viable (e.g., Civano et al. 2010; Robinson et al. 2010; Steinhardt et al. 2012; Koss et al. 2014; Markakis et al. 2015; Kalfountzou et al. 2017).

Recently, we found that the radio-loud quasar 3C 186 ( $z = 1.068$ ) displays all of the expected properties of a kicked active SMBH (Chiaberge et al. 2017). The *Hubble Space Telescope* (HST) image taken with WFC3-IR at  $\sim 1.4 \mu\text{m}$  clearly shows that the quasar does not reside at the center of the host galaxy, which appears to be a massive, relatively relaxed elliptical located at the center of a well-studied X-ray cluster of galaxies (Siemiginowska et al. 2005, 2010). Despite the complexity of its spectrum, we measured significant velocity offsets between the UV broad ( $\text{Ly}\alpha$ , C IV, C III, and Mg II) and the narrow lines. However, the available information did not allow us to definitely rule out other interpretations such as, e.g., a chance superposition of a large elliptical with an under-massive quasar host galaxy and/or the presence of significant outflows in the quasar spectrum that may mimic the measured offsets. Prominent outflows have been observed in other quasars, but they are typically seen in either the broad high ionization lines (e.g., Shen et al. 2016) or in narrow lines such as [O III]5007 in the most powerful quasars known (e.g., Vietri et al. 2018). Even if these alternative explanations seem to be unlikely for reasons that are extensively discussed in Chiaberge et al. (2017), it is extremely important to find independent confirmation of this GW recoiling black hole candidate.

In this work, we focus on one specific test that may shed further light on the structure of the emission-line systems in 3C 186. We present the results of our integral field spectroscopy observations taken with the Keck telescope and OSIRIS. The main goal of these observations is to establish the spatial location of the narrow emission-line features with respect to the location of the quasar. Are the narrow lines produced co-spatially with the quasar’s continuum point source? Are lines of different widths/velocities produced in the same region? Can we spatially separate outflowing components and find evidence for quasar feedback in this source? Does the broad  $\text{H}\beta$  line show the same offset as the UV permitted lines?

In Section 2 we describe the observations and the data reduction; in Section 3 we present the results, we discuss our findings in Section 4, and in Section 5 we draw conclusions.

Throughout the paper, the systemic redshift of the target is assumed to be  $z_s = 1.0685$ , as derived in Chiaberge et al. (2017) based on both UV absorption lines and low-ionization narrow emission lines. We use the following cosmological parameters throughout the paper:  $H_0 = 69.6 \text{ km s}^{-1} \text{ Mpc}^{-1}$ ,  $\Omega_M = 0.286$ ,  $\Omega_\lambda = 0.714$ .

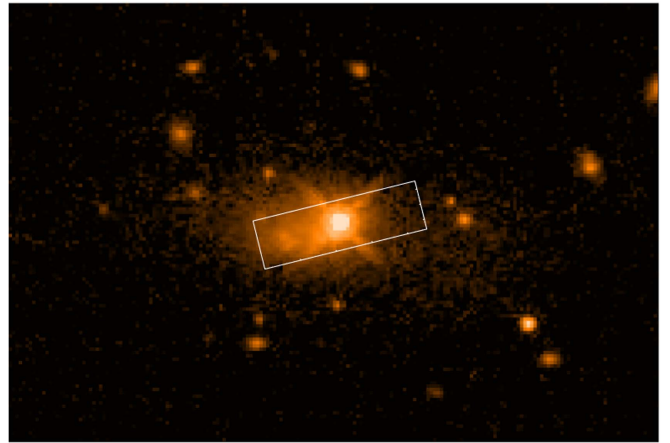


**Figure 1.** OSIRIS field of view ( $1.6'' \times 6.4''$ , corresponding to  $\sim 13 \text{ kpc} \times \sim 52 \text{ kpc}$ , at the distance of the target) overlaid onto the *HST*/WFC3-IR F140W image of 3C 186 (adapted from Chiaberge et al. 2017).

## 2. Observations and Data Reduction

The observations were performed on 2016 November 15 with OSIRIS (Larkin et al. 2006) and the Keck Laser Guide Star Adaptive Optics System. We utilized the  $Z_{bb}$  filter, which samples the range of wavelengths between 999 and 1176 nm. The scale used is  $0.1'' \text{ pixel}^{-1}$ , and the corresponding field of view is  $1.6'' \times 6.4''$ . The tip-tilt star correction was carried out using the quasar itself. The observations were performed using a standard A-B-A-B sequence, each with an exposure time of 900 s. We collected a total of seven exposures on the target for a total of 6300 s. A standard star for telluric correction was also observed for 10 s.

The data reduction was performed using the OSIRIS data reduction pipeline (ODRP) v4.0.0 following the procedures outlined in the ODRP Cookbook.<sup>5</sup> The steps include combining the sky exposures to make a sky image, reducing the telluric star data, performing a basic reduction of the target and producing a data cube, correcting sky subtraction to remove residual background, and correct for telluric absorption. For the reduction of the telluric star we assumed a blackbody temperature of 10,000 K.

In Figure 1 (left) we show the OSIRIS field of view overlaid onto the *HST* WFC3/IR image of the target (Chiaberge et al. 2017).

The absolute astrometry of the Keck data cube was significantly off ( $\sim 0.5 \text{ arcmin}$ ), most likely because of an error in the CRVAL keywords (i.e., the coordinates of the reference pixel). Therefore, we use the collapsed continuum image to register the OSIRIS data on the world coordinate system (WCS) of the *HST* image. We make the reasonable assumption that the point source seen in the *HST* data (i.e., the quasar) is the continuum source in Keck/OSIRIS.

The measured FWHM of the continuum source in the spectral region between 1040 and 1150 nm is  $0.55''$ , which we assume as the angular resolution of our data set at that wavelength. In the following, we will refer to this component simply as the quasar.

We performed a rough flux calibration by cross-calibrating the OSIRIS spectra with our Palomar TripleSpec spectroscopic observations of the same target (Chiaberge et al. 2017). However, the various line components and the continuum

<sup>5</sup> [https://www2.keck.hawaii.edu/inst/osiris/drp\\_cookbook.html](https://www2.keck.hawaii.edu/inst/osiris/drp_cookbook.html)

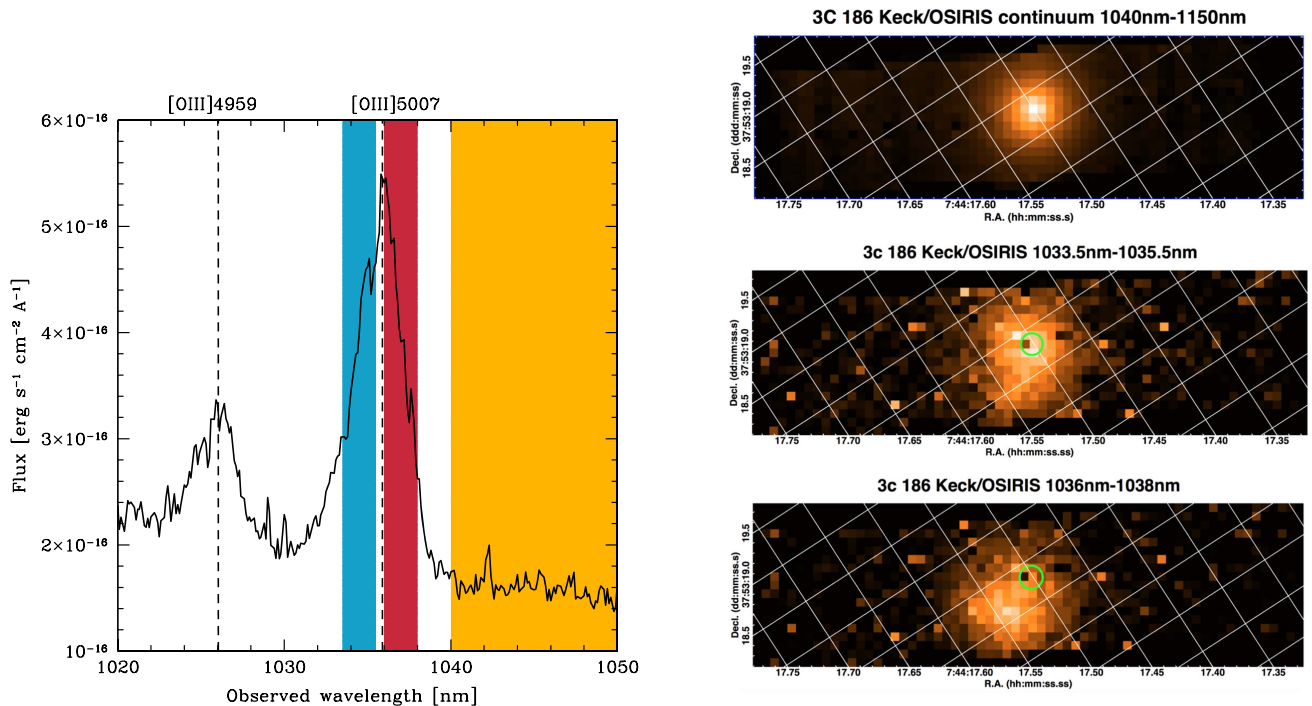


**Figure 2.** Left: Keck/OSIRIS spectrum of the region of the [O III]4959,5007 doublet extracted from a region of  $r = 6$  spaxels ( $r = 0''.6$ ) centered on the centroid of the continuum source. The colored areas refer to the collapsed images shown in the right panel. Dashed lines indicate the redshifted wavelengths of the lines at the systemic redshift  $z_s = 1.0685$ . Right: Keck/OSIRIS collapsed images of three different spectral regions. We show that the continuum emission between 1040 and 1150 nm (top, yellow shaded area in the left figure), continuum-subtracted blue side of the [O III]5007 line between 1033.5 and 1035.5 nm (center), and continuum-subtracted red side of the same line between 1036 and 1038 nm (bottom). The green circles in the center and bottom panels indicate the centroid of the continuum source.

emission are not co-spatial, and the spectra extraction regions do not include the entire point-spread function (PSF). Therefore, we only report flux densities in physical units where those represent a relatively accurate estimate of the aperture-corrected values (e.g., in Figure 2, left panel). Note that the aim of this work is not limited by the lack of an accurate flux calibration, since we are mainly focused on the offset and the spatial location of each line component.

To register the data cube onto the WCS of the *HST* observations and produce collapsed images we utilize the *GAIA Starlink* software (Draper et al. 2014). To extract spectra at different locations we use QFitsview (Ott 2012) with the *median* option.

### 3. Results

#### 3.1. Wavelength-dependent Morphology

The source presents a complex structure and its morphology varies depending on the observing wavelength. The target is unresolved in the spectral region redward of the [O III]5007 line, which is dominated by the quasar continuum. No stellar emission from the host galaxy is detected across the field of view. The FWHM of the object in the spectral region dominated by the broad  $H\beta$  emission line between 999 and 1004 nm is also consistent with a point source (FWHM =  $0''.59$ ).

The detected emission lines in the wavelength range covered by these observations are [O III]5007,4959 and  $H\beta$ , superimposed to a strong power-law continuum. The most interesting spectral region is that of the [O III]5007 line, which shows a complex line profile and morphology.

We first extract the spectrum from a relatively large region with radius  $r = 6$  spaxels (corresponding to  $0''.6$ , i.e.,

approximately equal to the seeing). The center of the extraction region is fixed at the spatial location of the quasar, i.e., on the centroid of the continuum emission as measured from the collapsed image between 1040 and 1150 nm. The spectrum is shown in the left panel of Figure 2, limited to the region of the [O III]4959,5007 doublet. The [O III]5007 line profile can be decomposed into possibly two narrow components and a blue wing. These line components will be further discussed in the following (see Section 3.2). We derive three collapsed images from the interesting spectral regions in which the signal-to-noise ratio (S/N) is sufficient to provide a meaningful spatial analysis. We show the results in the right panel of Figure 2: (i) continuum emission redward of the [O III]5007 line, top panel. Part of this continuum spectral region is shown by the yellow area in the spectrum reported in the left panel of the figure; (ii) continuum-subtracted blue side of the [O III]5007 line, central panel (blue area in the left panel); (iii) continuum-subtracted red side of the [O III]5007 line, bottom panel (red area in the left panel). The width of each slice derived across the [O III] line (i.e., regions ii and iii) corresponds to a velocity width of  $\sim 600 \text{ km s}^{-1}$ .

The three spectral components correspond to three different regions of the target. We utilize SExtractor within *GAIA/Starlink* for object detection. The FWHM of each source is also derived using the same software. As already pointed out above, the continuum source corresponds to the smallest observed structure and it is assumed to be spatially unresolved. The blue side of the [O III] line is emitted in a region apparently centered on the quasar, but its FWHM is  $\sim 1''.6$ , i.e., significantly larger than the PSF. The red side of the same line is also resolved, and most interestingly it is clearly off-nuclear. Its brightest area is located  $\sim 0''.5$  southeast of the quasar.

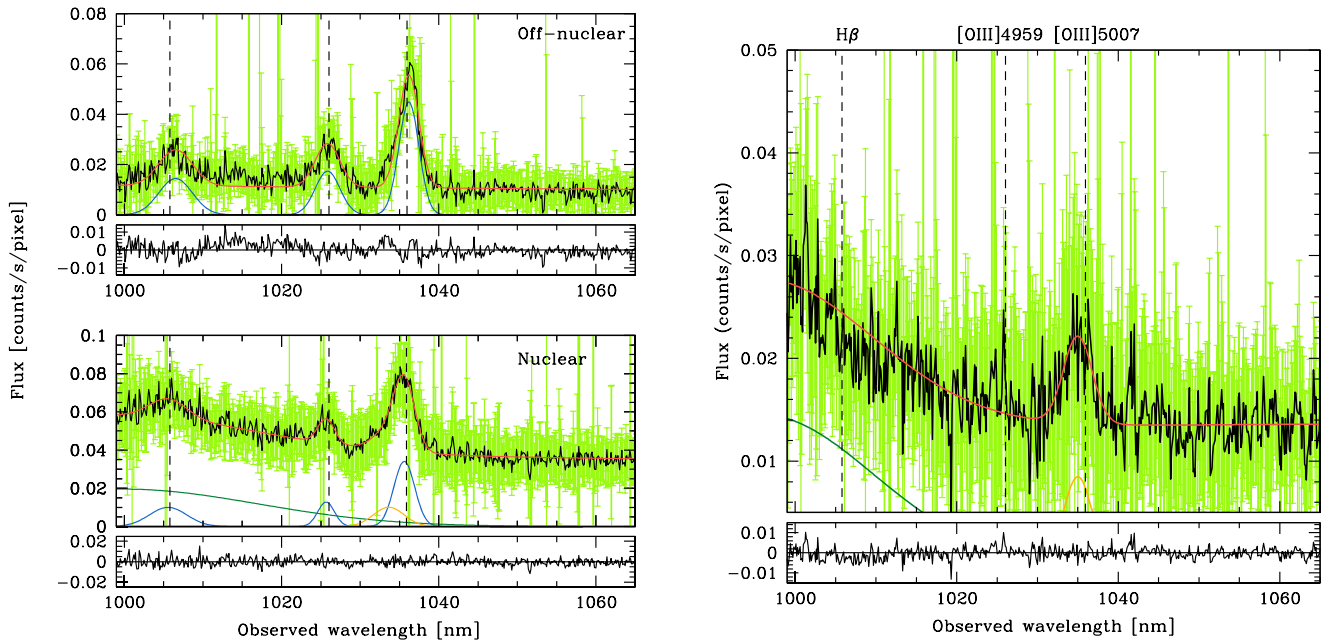


**Figure 3.** Left: nuclear and off-nuclear spectra are shown in the bottom and top panels, respectively. The nuclear spectrum is extracted from a region centered on the centroid of the continuum source. The off-nuclear spectrum is extracted from the region corresponding to the extended NLR located  $\sim 0''.5$  southeast of the quasar (see Figure 2, bottom-right panel). Right: nuclear spectrum obtained by subtracting an annulus of width  $d = 2$  spaxels from the central  $r = 2$  spaxels centered on the quasar. Residuals after spectral model subtraction are shown below each spectrum. The range shown in the residuals box corresponds to the  $1\sigma$  error.

We also attempted to derive a collapsed image for the bluer region of [O III]5007 between 1031 and 1033 nm, to determine the spatial location and size of the blue wing of such a line. The derived continuum-subtracted source is only detected at a level of  $\lesssim 2.5\sigma$  in that wavelength range, and thus the spatial extension cannot be measured robustly with this method. In the following, we derive more information on this component from the analysis of the nuclear and off-nuclear spectra.

It is worth noting that velocity and dispersion maps for these observations do not provide any useful information. This is likely because of both the complex nature of the spectrum, in which multiple lines are heavily blended, and the low S/N.

### 3.2. Nuclear and Off-nuclear Spectral Fits

We fit spectra extracted at different positions using the *Specfit* tool in *IRAF*. We utilize a power-law component and a collection of Gaussian profiles to fit each line of interest. The parameters are then successively freed and optimized through a maximum of 100 iterations using a combination of the *Simplex* and *Marquardt* minimization algorithms. The optimal parameters for each line are determined until convergence is achieved. The initial guess on the fit parameters is made by setting the parameters to reasonable values. We then allow the parameters to vary until convergence is achieved, without imposing any constraints on either the central wavelength or the FWHM of each line.

In Figure 3 (left, bottom panel) we show the extracted spectrum of the central region (i.e.,  $r = 1$  pixel centered on the centroid of the continuum source, at spaxel coordinates 11, 32). Errors (light green bars) are derived from the error array of each spaxel in the FITS data cube, and added in quadrature. By comparing the errorbars with the dispersion of the data points we think that the errors derived from the data cube are significantly overestimated.

The nuclear [O III]5007 line profile clearly shows a blue wing, and the  $H\beta$  line shows both a narrow and a broad component. We fit the spectrum using five Gaussian components: two for [O III]5007, one for [O III]4959, and two for  $H\beta$  (narrow and broad). Note that the [O III]5007 and 4959 lines are expected to show exactly the same components while in our model we only include one component for the fainter [O III] 4959 line, for the sake of simplicity. A model using a single line is sufficient because of the lower S/N in the spectral region covered by this line. The inclusion of any additional components fixed at the (rescaled) values derived for the [O III] 5007 line is a viable option, but it does not result in any additional information.

The results of the best fit are shown in Table 1. The central wavelengths of the two components of the [O III]5007 line are offset with respect to the systemic redshift  $z_s$  by  $-100$  and  $-670$  km s $^{-1}$ . The former component is narrow (FWHM  $\sim 900$  km s $^{-1}$ ) and the latter is slightly broader (FWHM  $\sim 1300$  km s $^{-1}$ ). The narrow component of the  $H\beta$  line also shows a small blueshift that is consistent with that of the narrow component of [O III]5007. The broad  $H\beta$  line (FWHM  $\sim 12,000$  km s $^{-1}$ ) is only partially included in the wavelength range covered by OSIRIS and the  $Z_{bb}$  filter. The model clearly shows that the line is significantly blueshifted ( $-1790 \pm 390$  km s $^{-1}$ ). The significance of such a blueshift with respect to the systemic redshift  $z_s$  is thus  $4.6\sigma$ .

In Figure 3 (left, top panel) we show the off-nuclear spectrum extracted from a circular region of radius  $r = 1$  spaxels centered at the peak of the off-nuclear emission at coordinates (7, 35). In this case we only need three Gaussian lines to achieve a satisfactory fit. The best fit shows that the most prominent line (i.e., [O III]5007) is slightly redshifted ( $+75 \pm 11$  km s $^{-1}$ ). Note that the region of extraction of this off-nuclear spectrum is still within the area covered by the PSF wings of the nuclear component. Therefore, the spectral region between  $H\beta$  and [O III]4959 is most likely contaminated by the

**Table 1**  
Emission Lines Best-fit Parameters

Line	Observed Wavelength $\lambda$ (nm)	Err.	Redshift $z$	Err.	Offset ( $\text{km s}^{-1}$ )	Err.	FWHM ( $\text{km s}^{-1}$ )	Err.
(1)	(2)	(3)	(4)	(5)	(6)	(7)	(8)	(9)
Nuclear spectrum								
H $\beta$ (narrow)	1005.57	0.35	1.0679	0.0007	−82	104.0	1671	333
H $\beta$ (broad)	999.86	1.35	1.0562	0.0028	−1785	405.0	12067	1058
[O III]4959	1025.67	0.14	1.0678	0.0003	−107	41.0	730	93
[O III]5007 (narrow)	1035.61	0.13	1.0678	0.0003	−100	38.0	905	58
[O III]5007 (broad-ish)	1033.64	1.01	1.0639	0.0020	−670	293.0	1341	200
Off-nuclear spectrum								
H $\beta$ (narrow)	1006.52	0.18	1.0699	0.0004	200	54.0	1498	276
[O III]4959	1025.85	0.11	1.0681	0.0002	−54	32.0	1078	90
[O III]5007 (narrow)	1036.20	0.04	1.0690	0.0001	71	12.0	872	33
Annulus-subtracted nuclear spectrum								
H $\beta$ (broad)	996.01	1.15	1.0483	0.0024	−2933	346.0	9692	486
[O III]5007 (broad-ish)	1034.99	0.21	1.0657	0.0004	−279	60.0	1213	163

broad nuclear component of the H $\beta$  line. Similarly, the continuum detected redward of the [O III]5007 line is most likely due to the PSF wings of the quasar continuum emission.

In the right panel of Figure 3 we show the spectrum obtained by subtracting an annulus of width  $d = 2$  spaxels just outside the nuclear spectrum extracted from a circular region of aperture  $r = 2$  spaxels, centered on the brightest pixel of the continuum source. The narrow components of all lines are no longer present, and only the broad H $\beta$  and the broad-ish [O III] 5007 (in addition to the nuclear continuum) are still visible. On the one hand, this confirms that the broad component of H $\beta$  is produced in an unresolved nuclear region. On the other hand, it indicates that the same holds for the broad-ish component of [O III].

We also fit the spectrum freezing the emission-line wavelength of the broad H $\beta$  to the value corresponding to the systemic redshift (1005.8 nm). The model reproduces the data less accurately at the blue end of the spectral coverage, and the  $\chi^2$  is worse than for the best-fit model, but a  $\chi^2$  difference test cannot completely rule out this scenario ( $P < 0.22$ ). On the contrary, for the nuclear spectrum shown in the right panel of Figure 3, the same test shows that a broad H $\beta$  line at the systemic redshift is completely inconsistent with the data. The  $\chi^2$  difference test shows that the confidence level is extremely high ( $P < 5 \times 10^{-5}$ ). While these results are clearly pointing toward a confirmation of an offset broad-line region (BLR), we stress that we cannot draw definitive conclusions based solely on these data. One major limitation of this data set is that the H $\beta$  line is not entirely sampled by these observations, in addition to the poor S/N in particular at the blue end of the spectral region covered by the  $z_{bb}$  filter.

In order to investigate whether the fit is unique and if different initial conditions may affect the best-fit solution for the broad H $\beta$  component in particular, we perform the test described in the following. We allow all of the parameters to be free to vary and we set the initial condition of the central wavelength for the broad H $\beta$  line at ten different values in the range  $\lambda_c = 997.0$ –1006.0 nm. We ran *Specfit* multiple times, using the *marquadt* minimization method for all the values in the range reported above, until convergence is achieved. The result is that for all of the initial conditions the solution

converges to values in the range  $\lambda_c = 997.4$ –999.7 nm, in agreement with the value reported in Table 1. The  $\chi^2$  values are all indistinguishable and the errors are between 2.5 nm (obtained for a best-fit value of  $\lambda_c = 999.7$  nm) and 0.7 (for  $\lambda_c = 997.9$  nm). Therefore, we conclude that the results of the fit are relatively robust even if the noise in that spectral region is high. Clearly, the lack of knowledge on the blue side of the line does not allow us to firmly conclude that the best fit is unique.

We also checked that rebinning the data set (in either the spatial or wavelength axes) does not produce more accurate results because of the reduced resolution.

It is possible that small calibration issues may affect the shape of the spectrum at its blue end. In order to test such a hypothesis, we average the spectra of four empty regions of the field of view of the detector, each with an aperture radius of  $r = 2$  spaxels. For wavelengths  $< 1005$  nm, i.e., at the very end of the bandpass, a small depression followed by a flux increase is observed (blue line in Figure 4). The amount of such an effect is  $0.005 \text{ c s}^{-1} \text{ pixel}^{-1}$ , peak to peak. This does not appear to be sufficient to significantly alter the shape of the extracted nuclear spectrum of the quasar. However, it is possible that the true line profile is slightly more peaked than reported in the extracted nuclear spectrum (green line in Figure 4), and it could be in fact similar to that derived for the annulus-subtracted nuclear spectrum shown in the right panel of Figure 3.

### 3.3. Energetics of the Outflow

Studies of the kinematics of the ionized gas around the central regions of active galaxies often reveal the presence of significant velocity offsets that are interpreted as evidence for winds (e.g., Liu et al. 2013; Ramos Almeida et al. 2017; Rupke et al. 2017; Sun et al. 2017). This phenomenon constitutes one of the expected manifestations of AGN feedback. One of the main goals of these observations is to study the presence of spatially displaced components of the narrow emission lines. As we noted above, we discovered three different emitting regions associated with different spectral components of the [O III]5007 line. It is likely that these red and blueshifted

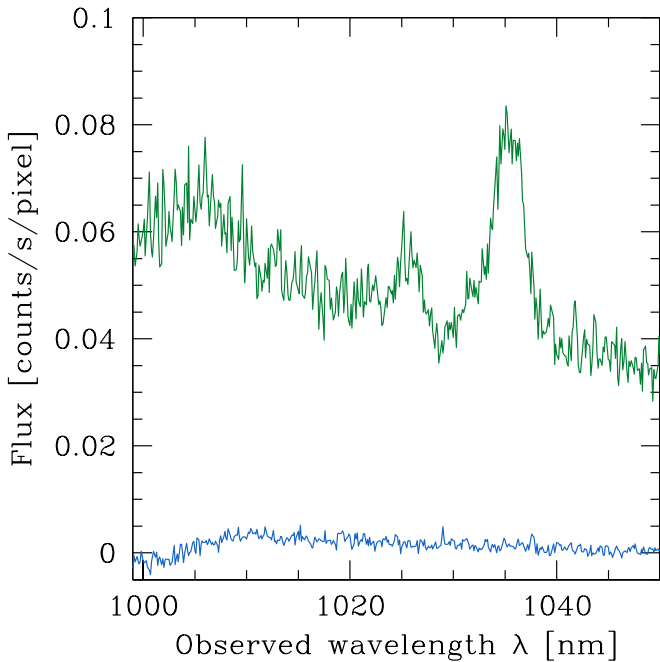


**Figure 4.** Average background spectrum extracted from four different empty regions of the detector, each with an aperture radius of  $r = 2$  spaxels (blue line), to investigate possible calibration issues at the blue end of the detector sensitivity band. For comparison, the green line shows the nuclear spectrum of 3C 186 (also shown in Figure 3).

features are signatures of the presence of winds powered by the active nucleus. It is interesting to compare the properties of such features with other quasar-powered winds to determine whether 3C 186 is a typical object or it presents significant peculiarities in its narrow emission-line region (NLR) structure, possibly because of its recoiling black hole.

We derive the maximum velocity  $v_{\max}$ , mass rate  $\dot{M}$ , and kinetic power  $L_{\text{kin}}$  of the outflow using the formulae reported in Carniani et al. (2015) and Bischetti et al. (2017). These authors studied samples of high-redshift ( $z \sim 2.3\text{--}3.5$ ) hyperluminous ( $L_{\text{bol}} \sim 10^{47}\text{--}10^{48}$  erg s $^{-1}$ ) quasars and found relatively broad (FWHM  $\sim 1000\text{--}2000$  km s $^{-1}$ ) components of the [O III]5007 emission line. The maximum velocity of the outflow is defined as  $v_{\max} = 2\sigma + |\Delta v|$ , where  $\sigma$  is the dispersion of the broad component of the [O III] line, and  $\Delta v$  is the velocity offset of that component with respect to the systemic redshift. For 3C 186,  $v_{\max} = 1810$  km s $^{-1}$ . The mass outflow rate is  $3300 M_{\odot} \text{ yr}^{-1}$ , using formula (4) in Bischetti et al. (2017) and assuming the same parameters as those authors except for a slightly smaller size of the emission-line region (i.e., 4.8 kpc instead of 7 kpc) because the higher spatial resolution of our Keck data allow us to set a slightly more stringent limit to the spatial scale.

The derived kinetic power is thus  $L_{\text{kin}} \sim 3 \times 10^{45}$  erg s $^{-1}$ . This corresponds to  $\sim 4\%$  of the bolometric luminosity for this object, which is  $L_{\text{bol}} = 7.5 \times 10^{46}$  erg s $^{-1}$ , as estimated from the total [O III] line luminosity (Chiaberge et al. 2017).

Interestingly, Bisogni et al. (2017) found an inverse dependency between the equivalent width (EW) of the [O III] 5007 line and the velocity offset of the blue component of the same line in a large sample of SDSS quasar. Objects with large EWs display smaller velocity offsets. For 3C 186, the EW as measured from the full aperture spectrum is  $\sim 90$ , while the offset is  $-670$  km s $^{-1}$ . This is about a factor of six larger than

the offset displayed by SDSS quasars with the same EW([O III]). The same holds for the offset of the main component of [O III]. Our measured value of  $-100$  km s $^{-1}$  is  $\sim 5$  times larger than that observed in SDSS quasars. However, as discussed below, we stress that our target is significantly more powerful than the SDSS quasars studied in Bisogni et al. (2017).

#### 4. Discussion

The Keck/OSIRIS IFU observations we present in this paper show three important properties of the target: (i) 3C 186 displays strong emission lines with multiple components; (ii) the emission-line region has a complex morphology, similar to that observed in other powerful quasars (e.g., Liu et al. 2013; Carniani et al. 2015); (iii) and the broad H $\beta$  line is blueshifted with respect to the systemic redshift.

The three components of the [O III]5007 emission line are produced in spatially distinct regions of the source. The most prominent component is redshifted by  $\sim 70$  km s $^{-1}$ , its FWHM is  $\sim 900$  km s $^{-1}$ , and it is produced in a spatially resolved off-nuclear region, at a distance of about  $0''.5$ , corresponding to a projected distance of  $\sim 4$  kpc. This feature is approximately located along the direction of the radio jet, which is oriented along a northwest–southeast direction. In low-frequency VLBI maps (Nan et al. 1992), the jet is one sided and the southeast side of the jet (i.e., the counter-jet) is not detected. Therefore any spatial association between the radio jet and the extended NLR cannot be firmly determined. However, it seems plausible that the redshifted component of the [O III] line could be produced in a relatively slow outflow possibly caused by jet-induced feedback, along the counter-jet (e.g., O’Dea 1998; O’Dea et al. 2003).

There are two blueshifted components of the [O III]5007 line. The former is narrow (FWHM  $\sim 900$  km s $^{-1}$ ), its offset is  $\sim -100$  km s $^{-1}$ , and the emitting region is resolved at the angular resolution of our IFU data. It is natural to identify such a component with the blueshifted counterpart of the narrow, redshifted feature of the same line. Its centroid is approximately aligned with the center of the quasar, therefore it must be produced in a region that is close, in projection, to the accretion disk. We stress that the angular resolution of our data corresponds to a few kpc, therefore we can only set an upper limit at a level that is allowed by our data.

The latter component is significantly broader (FWHM  $\sim 1300$  km s $^{-1}$ ), its emitting region is likely very compact (i.e., unresolved in our data), and its location coincides with the quasar continuum emission. The (blue-)shift displayed by such a component is  $\sim -700$  km s $^{-1}$ , therefore we conclude that this is a relatively fast wind produced even closer to the accretion disk as compared to the previously discussed features, but clearly still well outside of the BLR.

The second major result of these observations is the evidence in support of an extremely large blueshift of the emission lines emitted within the BLR. The H $\beta$  line is only partially included in our data, because at the redshift of the source its central wavelength is expected to be very close to the blue end of the sensitivity pass-band of the instrument. Despite the low S/N, we showed that the offset is significant, at a level of  $\sim 4.6\sigma$ . The best-fit value of the offset ( $v = -1790 \pm 400$  km s $^{-1}$ ) is consistent with the results of Chiaberge et al. (2017) based on the analysis of broad UV lines (Ly $\alpha$ , C IV, and Mg II,  $v = -2140 \pm 390$  km s $^{-1}$ ), within the margin of error. Note

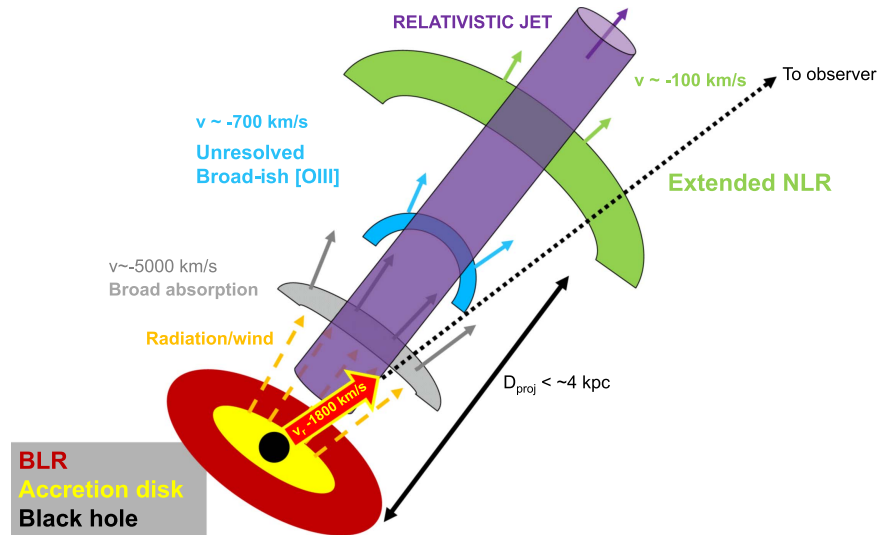


**Figure 5.** Schematic of the source as derived from the Keck/OSIRIS IFU data. Only the side of the AGN that faces the observer is reported. The green structure represents the slower (blueshifted) outflowing component seen in the [O III]5007 line. The blue feature is the  $\sim 700 \text{ km s}^{-1}$  outflow, and the gray shaded area represents the fast ionized outflow that produces the broad absorption lines observed in the UV spectrum (Chiaberge et al. 2017). The purple region is the relativistic jet. The black hole, the accretion disk, and the BLR are shown in black, yellow, and red, respectively. The radial velocity  $v_r$  of the black hole and the BLR along the line of sight is also shown with a thick red-colored arrow.

that those UV lines display a concave shape on the blue side, which was explained as due to a broad absorption feature. We cannot confirm such a feature to be present in the  $H\beta$  line with these data, since we are only sampling the red side of that line. Therefore, the results presented here are derived under the assumption of a symmetric Gaussian shape for each line.

Even if the statistical evidence for a  $\sim -1800 \text{ km s}^{-1}$  velocity offset is quite robust, we need to be extremely careful in drawing firm conclusions solely based on the results presented here. In fact, as we pointed out above, the peak of the line is located at the very end of the spectral region covered by our observations, and that might significantly affect the results because of the rather poor S/N in that region.

The fact that both the broad  $H\beta$  line and the broad-ish [O III] line are produced in an unresolved region of the AGN, co-spatial with the quasar continuum (at the resolution of our data), is also indicated by the nuclear spectrum shown in Figure 3 (right panel), obtained after subtracting off the emission from an annulus of  $d = 2$  spaxels just outside the nuclear aperture. It is remarkable that the only features that are left after that operation are the pure nuclear components, i.e., the quasar continuum, the broad line, and the fast outflowing component of the [O III] line.

The interpretation of our data is consistent with the picture envisaged by Chiaberge et al. (2017). The BLR, which is attached to the black hole and its accretion disk, is moving at a high velocity with respect to the gas at rest in the host galaxy of this quasar. This can be modeled as the result of a GW recoil kick, following the merger of two high-spin SMBH of comparable mass (Lousto et al. 2017).

The effect of AGN feedback is evident from both the morphology of the emission-line region and the spectral complexity of the spectral lines. The object seems to agree with other samples of similar sources, the only peculiarity being the rather large EW of the [O III] line with respect to the velocity of the outflows, as compared to what is observed in a large sample of SDSS quasars (Bisogni et al. 2017). However, 3C 186 is  $\sim 1$  dex more powerful than the brightest SDSS

quasar considered in Bisogni et al. (2017), in terms of AGN bolometric luminosity. Therefore, a comparison with a sample of quasars with similar power (e.g., such as that considered by Bischetti et al. 2017) is likely more appropriate to establish any peculiarities of our source. However, the fact that the general properties of the observed outflows match those of the general quasar population implies that radiation pressure onto the ISM of the host is likely producing the winds. Mechanical feedback seems ruled out because, in such a scenario, the added velocity of the kicked AGN would imply a faster wind with respect to non-recoiling AGNs of similar power.

In Figure 5 we show a schematic representing a possible geometry of the quasar and the structure of the NLR. The green feature is the slower [O III] component (the extended NLR) that lies on the side of the jet that points toward the observer. A similar feature (not shown in the figure) is also present on the opposite side of the accretion disk with respect to the observer (i.e., the mildly redshifted component of the [O III] line). Such a feature is likely located at a significantly larger distance from the black hole, to account for the observed spatial offset. The blue feature corresponds to the broad-ish [O III] component, which is most likely located within a few kpc from the black hole. The gray shaded region represents the fast ionized outflow that produces the broad absorption lines observed in the UV spectrum (Chiaberge et al. 2017). The purple cylinder represents the direction of propagation of the radio jet. The dashed yellow arrows represent radiation pressure exerted onto the host galaxy ISM, which is most likely producing the observed winds. At larger distances, it is possible that the radio jet also contributes to this feedback process.

## 5. Conclusions

We presented Keck/OSIRIS IFU data of the radio-loud quasar 3C 186 aimed at studying both the structure and kinematics of the narrow-line region of the source. *HST* observations first published in Chiaberge et al. (2017) showed that the quasar is offset with respect to the center of the host galaxy by  $\sim 11$  kpc. Rest-frame UV spectra presented in that

paper also show a significant ( $\sim 2100 \text{ km s}^{-1}$ ) velocity offset between the broad and narrow lines. The observations were interpreted as the result of a GW kick resulting from a merger of two SMBH that happened  $\sim 5 \times 10^6$  years ago. Recoiling black holes originated by GW kicks are extremely important objects because of their bearings on our knowledge of how massive black holes interact with each other, possibly merge, and grow in size. Finding confirmed GW kicked black holes is also crucially important to rule out the so-called final parsec problem, which might prevent SMBH from merging after galaxy merger events, thus limiting the possibility that GWs emitted by such a phenomenon can be detected with PTA experiments and by future space missions such as LISA. These Keck observations do not constitute a definitive proof that the interpretation as a GW recoiling black hole for this object is correct. However, these data appear to support such a scenario. In addition, the effects of AGN feedback onto the galaxy ISM are clearly visible.

We showed that there are three different spectral components, each associated with a spatially distinct region of the emission-line region. The analysis of the profile of the [O III] 5007 line shows that a relatively slow ( $v \sim 100 \text{ km s}^{-1}$ ) outflow is present on large scales ( $>$  a few kpc from the black hole). This outflow is both blueshifted and redshifted, and each component is associated with a spatially distinct region, roughly aligned with the direction of the relativistic jet. A faster, blueshifted ( $v \sim -700 \text{ km s}^{-1}$ ) outflowing component that is co-spatial with the quasar center is also seen. The properties of the outflows observed in this quasar are consistent with those seen in other quasar samples, although some peculiarities are present. Based on the observed properties, we conclude that radiation pressure onto the ISM is the most likely origin for this feedback process.

The broad-line region, which is sampled in our observations by the  $H\beta$  line, is significantly blueshifted with respect to the narrow emission lines. The  $H\beta$  line is not fully sampled by our data, since its central wavelength apparently lies at the blue end of the filter pass-band. However, the best-fit model shows a statistically significant velocity offset of  $\sim 1800 \text{ km s}^{-1}$ , i.e., consistent with the findings of Chiaberge et al. (2017) based on permitted UV lines.

Spectroscopic observations sampling the full  $H\beta$  broad emission line will be key to definitely confirm the GW recoiling black hole scenario. In order to provide final evidence in favor (or against) for this interpretation, *James Webb Space Telescope (JWST)* IFU data should be obtained using the NIRSPEC IFU instrument to fully sample the  $H\beta$  spectral region and achieve a significantly higher spatial resolution ( $0''.1$  versus  $0''.5$  provided by the observations presented here). Deep imaging with *HST* and *JWST* information will be extremely important to further constrain the absence of a second (under-massive) galaxy around the quasar, as discussed at length in Chiaberge et al. (2017). Finally, with *JWST* it will also be possible to detect spectral features from stars in the host galaxy, thus providing an independent measure of the redshift of the host.

The authors wish to thank the anonymous referee for insightful comments that helped to significantly improve the paper. M.C. thanks Marshall Perrin for useful hints on the data reduction. The data presented herein were obtained at the W. M. Keck Observatory, which is operated as a scientific

partnership among the California Institute of Technology, the University of California, and the National Aeronautics and Space Administration. The observatory was made possible by the generous financial support of the W. M. Keck Foundation. The authors wish to recognize and acknowledge the very significant cultural role and reverence that the summit of Maunakea has always had within the indigenous Hawaiian community. We are most fortunate to have the opportunity to conduct observations from this mountain. Some of the data presented here are based on observations made with the NASA/ESA *HST*, obtained from the data archive at the Space Telescope Science Institute (STScI). STScI is operated by the Association of Universities for Research in Astronomy, Inc. under NASA contract NAS 5-26555.

### ORCID iDs

Marco Chiaberge  <https://orcid.org/0000-0003-1564-3802>  
 Grant R. Tremblay  <https://orcid.org/0000-0002-5445-5401>  
 Alessandro Capetti  <https://orcid.org/0000-0003-3684-4275>  
 Colin Norman  <https://orcid.org/0000-0002-5222-5717>

### References

- Amaro-Seoane, P., Audley, H., Babak, S., et al. 2017, arXiv:1702.00786  
 Begelman, M. C., Blandford, R. D., & Rees, M. J. 1980, *Natur*, **287**, 307  
 Bischetti, M., Piconcelli, E., Vietri, G., et al. 2017, *A&A*, **598**, A122  
 Bisogni, S., Marconi, A., & Risaliti, G. 2017, *MNRAS*, **464**, 385  
 Blecha, L., Cox, T. J., Loeb, A., & Hernquist, L. 2011, *MNRAS*, **412**, 2154  
 Blecha, L., Sijacki, D., Kelley, L. Z., et al. 2016, *MNRAS*, **456**, 961  
 Bortolas, E., Gualandris, A., Dotti, M., Spera, M., & Mapelli, M. 2016, *MNRAS*, **461**, 1023  
 Campanelli, M., Lousto, C. O., Zlochower, Y., & Merritt, D. 2007, *PhRvL*, **98**, 231102  
 Carniani, S., Marconi, A., Maiolino, R., et al. 2015, *A&A*, **580**, A102  
 Chiaberge, M., Ely, J. C., Meyer, E. T., et al. 2017, *A&A*, **600**, A57  
 Civano, F., Elvis, M., Lanzuisi, G., et al. 2010, *ApJ*, **717**, 209  
 Draper, P. W., Gray, N., Berry, D. S., & Taylor, M. 2014, GAIA: Graphical Astronomy and Image Analysis Tool, Astrophysics Source Code Library, ascl:1403.024  
 Dvorkin, I., & Barausse, E. 2017, *MNRAS*, **470**, 4547  
 Ferrarese, L., & Merritt, D. 2000, *ApJL*, **539**, L9  
 Gebhardt, K., Bender, R., Bower, G., et al. 2000, *ApJL*, **539**, L13  
 Gerosa, D., Hébert, F., & Stein, L. C. 2018, *PhRvD*, **97**, 104049  
 Healy, J., & Lousto, C. O. 2018, arXiv:1801.08162  
 Hobbs, G. 2013, *CQGr*, **30**, 224007  
 Kalfountzou, E., Santos Lleo, M., & Trichas, M. 2017, *ApJL*, **851**, L15  
 Khan, F. M., Just, A., & Merritt, D. 2011, *ApJ*, **732**, 89  
 Khan, F. M., Preto, M., Berczik, P., et al. 2012, *ApJ*, **749**, 147  
 Komossa, S. 2012, *AdAst*, **2012**, 364973  
 Koss, M., Blecha, L., Mushotzky, R., et al. 2014, *MNRAS*, **445**, 515  
 Kramer, M., & Champion, D. J. 2013, *CQGr*, **30**, 224009  
 Larkin, J., Barczyns, M., Krabbe, A., et al. 2006, *Proc. SPIE*, **6269**, 62691A  
 Liu, G., Zakamska, N. L., Greene, J. E., Nesvadba, N. P. H., & Liu, X. 2013, *MNRAS*, **436**, 2576  
 Loeb, A. 2007, *PhRvL*, **99**, 041103  
 Lousto, C. O., Zlochower, Y., & Campanelli, M. 2017, *ApJL*, **841**, L28  
 Madau, P., & Quataert, E. 2004, *ApJL*, **606**, L17  
 Markakis, K., Dierkes, J., Eckart, A., et al. 2015, *A&A*, **580**, A11  
 Mayer, L. 2017, *JphCS*, **840**, 012025  
 McLaughlin, M. A. 2013, *CQGr*, **30**, 224008  
 Merritt, D., Milosavljević, M., Favata, M., Hughes, S. A., & Holz, D. E. 2004, *ApJL*, **607**, L9  
 Middleton, H., Chen, S., Del Pozzo, W., Sesana, A., & Vecchio, A. 2018, *NatCo*, **9**, 573  
 Milosavljević, M., & Merritt, D. 2003, *ApJ*, **596**, 860  
 Nan, R., Cai, Z., Inoue, M., et al. 1992, *PASJ*, **44**, 273  
 O’Dea, C. P. 1998, *PASP*, **110**, 493  
 O’Dea, C. P., de Vries, W. H., Koekemoer, A. M., et al. 2003, *PASA*, **20**, 88  
 Ott, T. 2012, QFitsView: FITS file viewer, Astrophysics Source Code Library, ascl:1210.019  
 Preto, M., Berentzen, I., Berczik, P., & Spurzem, R. 2011, *ApJL*, **732**, L26

- Ramos Almeida, C., Piqueras López, J., Villar-Martín, M., & Bessiere, P. S. 2017, [MNRAS](#), **470**, 964
- Rasskazov, A., & Merritt, D. 2017, [PhRvD](#), **95**, 084032
- Robinson, A., Young, S., Axon, D. J., Kharb, P., & Smith, J. E. 2010, [ApJL](#), **717**, L122
- Rupke, D. S. N., Gültekin, K., & Veilleux, S. 2017, [ApJ](#), **850**, 40
- Shannon, R. M., Ravi, V., Lentati, L. T., et al. 2015, [Sci](#), **349**, 1522
- Shen, Y., Brandt, W. N., Richards, G. T., et al. 2016, [ApJ](#), **831**, 7
- Siemiginowska, A., Burke, D. J., Aldcroft, T. L., et al. 2010, [ApJ](#), **722**, 102
- Siemiginowska, A., Cheung, C. C., LaMassa, S., et al. 2005, [ApJ](#), **632**, 110
- Steinhardt, C. L., Schramm, M., Silverman, J. D., et al. 2012, [ApJ](#), **759**, 24
- Sun, A.-L., Greene, J. E., & Zakamska, N. L. 2017, [ApJ](#), **835**, 222
- Vietri, G., Piconcelli, E., Bischetti, M., et al. 2018, [arXiv:1802.03423](#)
- Volonteri, M., & Madau, P. 2008, [ApJL](#), **687**, L57